

# Relative Entropy Regularized TDLAS Tomography for Robust Temperature Imaging

Yong Bao<sup>1</sup>, Member, IEEE, Rui Zhang<sup>1</sup>, Godwin Enemali<sup>1</sup>, Member, IEEE, Zhang Cao<sup>1</sup>, Member, IEEE, Bin Zhou<sup>1</sup>, Hugh McCann<sup>1</sup>, and Chang Liu<sup>1</sup>, Member, IEEE

**Abstract**—Tunable diode laser absorption spectroscopy (TDLAS) tomography has been widely used for *in situ* combustion diagnostics, yielding images of both species concentration and temperature. The temperature image is generally obtained from the reconstructed absorbance distributions for two spectral transitions, i.e., two-line thermometry. However, the inherently ill-posed nature of tomographic data inversion leads to noise in each of the reconstructed absorbance distributions. These noise effects propagate into the absorbance ratio and generate artifacts in the retrieved temperature image. To address this problem, we have developed a novel algorithm, which we call Relative Entropy Tomographic ReConstruction (RETRO), for TDLAS tomography. A relative entropy regularization is introduced for high-fidelity temperature image retrieval from jointly reconstructed two-line absorbance distributions. We have carried out numerical simulations and proof-of-concept experiments to validate the proposed algorithm. Compared with the well-established simultaneous algebraic reconstruction technique (SART), the RETRO algorithm significantly improves the quality of the tomographic temperature images, exhibiting excellent robustness against TDLAS tomographic measurement noise. RETRO offers great potential for industrial field applications of TDLAS tomography, where it is common for measurements to be performed in very harsh environments.

**Index Terms**—Laser absorption spectroscopy, regularization, relative entropy, temperature imaging, tomography, two-line thermometry.

## I. INTRODUCTION

SINCE the first experimental demonstration of high-speed chemical species tomography [1], interest in tunable diode laser absorption spectroscopy (TDLAS) tomography has grown rapidly, with a focus on noninvasive imaging of critical combustion parameters, e.g., temperature [2]–[5], gas concentration [3]–[7], pressure [8], [9], and velocity [10], in reactive flows. High-fidelity temperature imaging is of critical interest, as the temperature distribution directly relates to heat transfer

and reveals combustion efficiency and temperature-dependent creation of pollutants, such as NO<sub>x</sub> and CO. Therefore, many articles on TDLAS tomography have focused on improving the accuracy and robustness of temperature imaging.

The widely adopted method in TDLAS tomography for temperature imaging is the so-called two-line strategy [11], where the absorbance distributions for two spectral transitions with different temperature-dependent line strengths are individually reconstructed, then the temperature image is retrieved from the ratio of the absorbances in each pixel of the region of interest (RoI). Alternatively, temperature images can be reconstructed by using spectra for multiple transitions, the so-called hyperspectral tomography (HT) [12], [13]. Although better accuracy and noise resistance can be achieved by HT, measurement of the necessary spectra requires expensive hardware, e.g., broadband lasers and detectors [5], and introduces high computational cost for data inversion. In contrast, the two-line strategy is cost-effective for temperature retrieval, placing minimal requirements on optical components and computing resources, and it is adopted in this article.

Temperature imaging using the two-line strategy requires the solution of two linear inverse problems by reconstructing, from the line-of-sight (LOS) TDLAS measurements, the absorbance distribution for each spectral feature. The inverse problems are inherently ill-posed due to the limited number of available LOS measurements and their inevitable uncertainties, leading to noise in each of the reconstructed absorbance distributions [14]. To mitigate the instability of the reconstructions, a variety of computational tomographic algorithms have been applied in TDLAS tomography, e.g., algebraic reconstruction technique (ART) [15], simultaneous ART (SART) [3], [16], Landweber algorithm [4], [17], and Tikhonov regularization [18], by formulating the inverse problem with a heuristically determined prior, e.g., smoothness of the true temperature distributions. Noise in the retrieved absorbance distributions, particularly in the denominator of the two-line ratio, propagates into the ratio and generates spike noise in the temperature image. To address this problem, we have developed a tomographic reconstruction algorithm using relative entropy regularization, and the algorithm is called Relative Entropy Tomographic ReConstruction (RETRO). The inverse problem of RETRO is solved by cone optimization, enabling high-fidelity temperature retrieval from jointly reconstructed two-line absorbance distributions. As well as using smoothness constraints, relative entropy regularization is imposed to directly penalize large values in

Manuscript received June 13, 2020; revised October 16, 2020; accepted November 1, 2020. Date of publication November 16, 2020; date of current version December 29, 2020. This work was supported in part by the U.K. Engineering and Physical Sciences Research Council under Platform Grant EP/P001661/1 and in part by the European Union under H2020 Contract JTI-CS2-2017-CFP06-ENG-03-16. The Associate Editor coordinating the review process was Dr. Chi-Hung Hwang. (Corresponding author: Chang Liu.)

Yong Bao, Rui Zhang, Godwin Enemali, Hugh McCann, and Chang Liu are with the School of Engineering, The University of Edinburgh, Edinburgh EH9 3JL, U.K. (e-mail: C.Liu@ed.ac.uk).

Zhang Cao is with the School of Instrumentation and Optoelectronic Engineering, Beihang University, Beijing 100191, China.

Bin Zhou is with the School of Energy and Environment, Southeast University, Nanjing 210096, China.

Digital Object Identifier 10.1109/TIM.2020.3037950

1557-9662 © 2020 IEEE. Personal use is permitted, but republication/redistribution requires IEEE permission.

See <https://www.ieee.org/publications/rights/index.html> for more information.

the ratio of two-line absorbance and therefore alleviates the spike noise in the tomographic images. The proposed RETRO algorithm promises to be highly beneficial for industrial applications of TDLAS tomography, e.g., gas turbine exhaust imaging [19] and power plant boiler diagnosis [20], where significant noise contamination of TDLAS measurements is common due to the harsh measurement environment. Recently, statistical inversion has been investigated by imposing *a priori* knowledge on the desired solution based on the framework of Bayesian statistics. The solution is then calculated based on the maximum *a posteriori* (MAP) estimation [21] or covariance estimation [22]. Although this article does not address statistical inversion techniques, the proposed relative entropy regularization can also be used in the statistical inversion framework.

## II. METHODS

### A. Formulation of TDLAS Tomography

When a laser beam at frequency  $\nu$  [cm<sup>-1</sup>] penetrates an absorbing gas sample on a path of length  $L$  [cm], a proportion of its intensity is absorbed. According to Beer's law, the wavelength-dependent absorbance can be defined as

$$\alpha(\nu) = \ln \frac{I_0(\nu)}{I_t(\nu)} = \int_0^L P(l)X(l)S_\nu(T(l))\phi(\nu, l)dl, \quad (1)$$

where  $I_0(\nu)$  and  $I_t(\nu)$  are the incident and transmitted laser intensities, respectively, and  $l$  is the position along the path.  $P(l)$  [atm] is the local total pressure,  $X(l)$  the local molar fraction of the absorbing species,  $T(l)$  [K] the local temperature,  $\phi(\nu, l)$  [cm] the line shape function, and  $S(T)$  [cm<sup>-2</sup>atm<sup>-1</sup>] the temperature-dependent line strength.

Since the line shape function can be normalized as  $\int_{-\infty}^{+\infty} \phi(\nu, l)d\nu \equiv 1$ , the path integral  $A_\nu$  can be formulated as

$$\begin{aligned} A_\nu &= \int_{-\infty}^{+\infty} \alpha(\nu) d\nu = \int_0^L P X(l) S_\nu(T(l)) dl \\ &= \int_0^L a_\nu(l) dl \end{aligned} \quad (2)$$

where  $a_\nu$  is the local density of the path integral.

For TDLAS tomography, (2) can be discretized as

$$\mathbf{A}_\nu = \mathbf{L} \mathbf{a}_\nu \quad (3)$$

where  $\mathbf{A}_\nu \in \mathbb{R}^{M \times 1}$  denotes the vector of path integrals obtained from  $M$  LOS-TDLAS measurements.  $\mathbf{L} \in \mathbb{R}^{M \times N}$  is the sensitivity matrix with its element  $l_{i,j}$  representing the length of the laser path segment for the  $i$ th laser beam passing through the  $j$ th pixel.  $i$  ( $i = 1, 2, \dots, M$ ) and  $j$  ( $j = 1, 2, \dots, N$ ) are the indices of laser beams and pixels, respectively.  $\mathbf{a}_\nu \in \mathbb{R}^{N \times 1}$  is the vector of the density of  $A_\nu$  with its elements  $a_{\nu,j} = P_j X_j S_\nu(T_j)$ .

### B. SART-Based TDLAS Tomographic Reconstruction

SART is one of the most well-established algorithms for hard-field tomography. This technique maintains the rapid convergence rate of the ART, while retaining the noise-suppression features of the simultaneous iterations

reconstruction technique (SIRT) [23]. In this article, SART is used as a representative tomographic algorithm and its performance is compared with the proposed RETRO.

Using the *a priori* information of smoothness, the two-line absorbance distributions,  $\mathbf{a}_{\nu 1}$  and  $\mathbf{a}_{\nu 2}$ , can be reconstructed by solving the following regularized least-squares problem:

$$\arg \min_{\mathbf{a}_\nu} \{ \|\mathbf{A}_\nu - \mathbf{L} \mathbf{a}_\nu\|_{\mathbf{W}}^2 + \lambda \|\mathbf{F} \mathbf{a}_\nu\|_2^2 \} \quad \text{s.t. } \mathbf{a}_\nu \geq \mathbf{0} \quad (4)$$

where  $\|\mathbf{F} \mathbf{a}_\nu\|_2^2$  is the first-order Tikhonov regularization term with a linear differential operator  $\mathbf{F}$ .  $\lambda$  is the empirically determined regularization parameter. The residual term  $\|\mathbf{A}_\nu - \mathbf{L} \mathbf{a}_\nu\|_{\mathbf{W}}^2$  is weighted per unit length of the laser path using  $\mathbf{W}$ , which is defined as

$$\mathbf{W} = \text{diag}(1/l_{\text{ray},1}, 1/l_{\text{ray},2}, \dots, 1/l_{\text{ray},M}), \quad (5)$$

where  $l_{\text{ray},i}$  denotes the length of the  $i$ th beam through the RoI

$$l_{\text{ray},i} = \sum_{j=1}^N l_{i,j}. \quad (6)$$

By utilizing adaptive step size  $\eta$ , and nonnegative projection operator  $\Pi_+(\cdot)$ , SART solves (4) iteratively as

$$\mathbf{a}_\nu^{k+1} = \Pi_+(\mathbf{a}_\nu^k + \eta \mathbf{C} \mathbf{L}^T \mathbf{W} (\mathbf{A}_\nu - \mathbf{L} \mathbf{a}_\nu^k) - \lambda \mathbf{C} \mathbf{F}^T \mathbf{F} \mathbf{a}_\nu^k) \quad (7)$$

where  $\Pi_+(\cdot)$  operates as  $\Pi_+(a_{\nu,j}) = \max(0, a_{\nu,j})$ .

$\mathbf{C}$  is the diagonal preconditioner defined as

$$\mathbf{C} = \text{diag}(1/l_{\text{pixel},1}, 1/l_{\text{pixel},2}, \dots, 1/l_{\text{pixel},N}) \quad (8)$$

where

$$l_{\text{pixel},j} = \sum_{i=1}^M l_{i,j}. \quad (9)$$

In each iteration,  $\eta$  is updated by back-tracking line search [24].

Finally, the temperature in the  $j$ th pixel,  $T_j$ , can be calculated by the two-line absorbance ratio,  $R_j$ , given by

$$R_j = \frac{a_{\nu 2,j}}{a_{\nu 1,j}} = \frac{S_{\nu 2}(T_j)}{S_{\nu 1}(T_j)}. \quad (10)$$

Equation (10) shows that the quality of the temperature image directly depends on the noise level of the two-line absorbance ratio. Although smoothness regularization is used in SART, the individually reconstructed  $\mathbf{a}_{\nu 1}$  and  $\mathbf{a}_{\nu 2}$  inevitably suffer from perturbations caused by the ill-posed nature of TDLAS tomography. Fig. 1 illustrates intuitively the resulting spike noise for each pixel in the temperature image. For these calculations, the inverse problem is formulated using the tomographic sensor and phantom 2 introduced in Section III-A below; TDLAS measurements are simulated with a signal-to-noise ratio (SNR) of 40 dB. The reconstructed and original  $a_{\nu 1,j}$  and  $a_{\nu 2,j}$  with their relative errors  $e_{\nu 1,j}$  and  $e_{\nu 2,j}$  in each pixel are shown in Fig. 1(a) and (b), respectively. Although the maximum values of  $e_{\nu 1}$  and  $e_{\nu 2}$  are 0.046 and 0.103, respectively, very large spike noise effects can be observed in the  $T_j$  values shown in Fig. 1(c), with a maximum relative error  $e_{T,j}$  of 1.51.

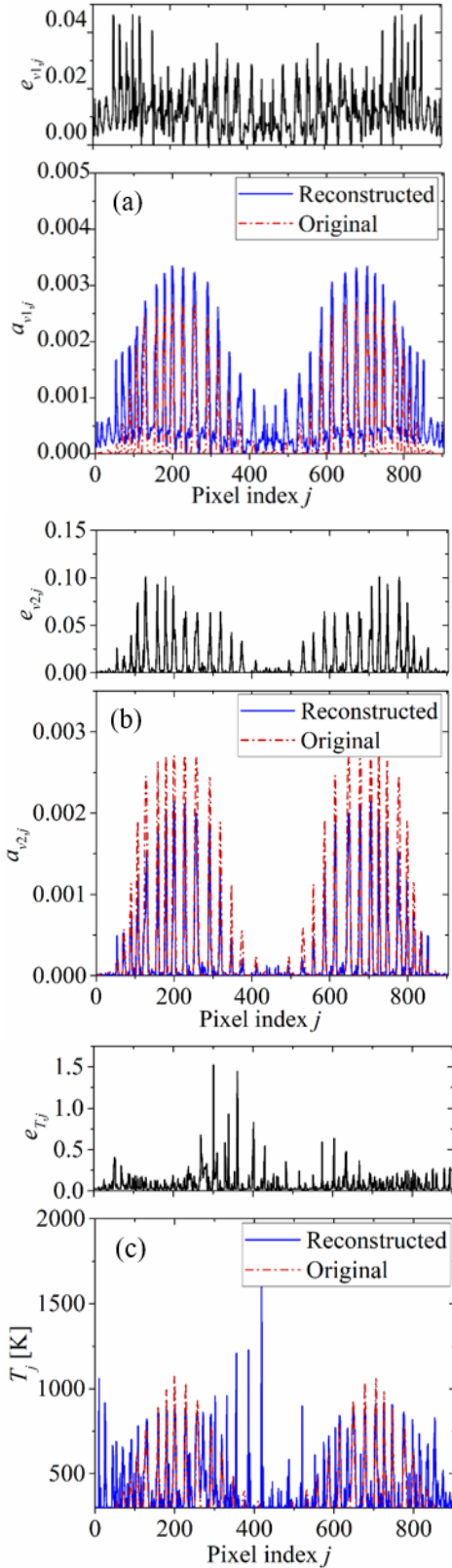


Fig. 1. Spike noise introduced in temperature reconstruction using SART. (a)–(c) Reconstructed and original absorbance  $a_{v1,j}$ ,  $a_{v2,j}$ , and temperature  $T_j$  in  $j$ th pixel with their relative errors  $e_{v1,j}$ ,  $e_{v2,j}$ , and  $e_{T,j}$ , respectively.

### C. RETRO-Based TDLAS Tomographic Reconstruction

The RETRO algorithm proposed here introduces a constraint that directly enforces the smoothness of the two-line

absorbance ratio. Both  $\mathbf{a}_{v1}$  and  $\mathbf{a}_{v2}$  are jointly reconstructed by solving the following inverse problem:

$$\begin{aligned} \min_{\mathbf{a}_{v1}, \mathbf{a}_{v2}} & \left\{ \left\| \begin{bmatrix} \mathbf{A}_{v1} \\ \mathbf{0} \end{bmatrix} - \begin{bmatrix} \mathbf{L}\mathbf{a}_{v1} \\ \gamma \mathbf{F}\mathbf{a}_{v1} \end{bmatrix} \right\|_2^2 + \left\| \begin{bmatrix} \mathbf{A}_{v2} \\ \mathbf{0} \end{bmatrix} - \begin{bmatrix} \mathbf{L}\mathbf{a}_{v2} \\ \gamma \mathbf{F}\mathbf{a}_{v2} \end{bmatrix} \right\|_2^2 \right\} \\ \text{s.t. } & \mathbf{a}_{v1} > \mathbf{0}, \mathbf{a}_{v2} > \mathbf{0}, \|\mathbf{a}_{v2} \cdot / \mathbf{a}_{v1}\|_2^2 < r \end{aligned} \quad (11)$$

where  $\gamma$  is the smoothness regularization parameter and  $r$  the ratio constraint parameter.

The constrained optimization problem in (11) can be reformulated into the following unconstrained problem using Lagrange's multipliers:

$$\begin{aligned} \min_{\mathbf{a}_{v1}, \mathbf{a}_{v2}} & \left\{ \left\| \begin{bmatrix} \mathbf{A}_{v1} \\ \mathbf{0} \end{bmatrix} - \begin{bmatrix} \mathbf{L}\mathbf{a}_{v1} \\ \gamma \mathbf{F}\mathbf{a}_{v1} \end{bmatrix} \right\|_2^2 + \left\| \begin{bmatrix} \mathbf{A}_{v2} \\ \mathbf{0} \end{bmatrix} - \begin{bmatrix} \mathbf{L}\mathbf{a}_{v2} \\ \gamma \mathbf{F}\mathbf{a}_{v2} \end{bmatrix} \right\|_2^2 \right. \\ & \left. + \mu \|\mathbf{a}_{v2} \cdot / \mathbf{a}_{v1}\|_2^2 \right\} \\ \text{s.t. } & \mathbf{a}_{v1} > \mathbf{0}, \mathbf{a}_{v2} > \mathbf{0} \end{aligned} \quad (12)$$

where  $\mu$  represents the two-line absorbance ratio regularization parameter. Unlike the smoothness regularization parameter  $\gamma$  for single-line absorbance, the selection of  $\mu$  has a direct impact on the reconstruction of line strength ratio and thus the temperature. A too large  $\mu$  will flatten the temperature peaks while a too small  $\mu$  cannot suppress the spike noise.

However, the regularization term  $\mu \|\mathbf{a}_{v2} \cdot / \mathbf{a}_{v1}\|_2^2$  is not convex [25], therefore it is generally difficult to use in the determination of the globally optimal solution for (12) [26]. To replace this regularization term, we developed a relative entropy function  $g(\mathbf{a}_{v2}, \mathbf{a}_{v1})$  that is jointly convex in terms of both  $\mathbf{a}_{v2}$  and  $\mathbf{a}_{v1}$  [27], as follows:

$$\begin{aligned} g(\mathbf{a}_{v2}, \mathbf{a}_{v1}) &= \begin{cases} (\mathbf{a}_{v2} + \mathbf{a}_{v1}) \circ \log(1 + \mathbf{a}_{v2} \cdot / \mathbf{a}_{v1}), & \text{if } \mathbf{a}_{v2}, \mathbf{a}_{v1} > \mathbf{0} \\ \mathbf{0}, & \text{if } \mathbf{a}_{v1} + \mathbf{a}_{v2} = \mathbf{0}, \\ & \mathbf{a}_{v1} \geq \mathbf{0} \\ +\infty, & \text{otherwise.} \end{cases} \end{aligned} \quad (13)$$

The relative entropy regularization term  $\|(\mathbf{a}_{v2} + \mathbf{a}_{v1}) \circ \log(1 + \mathbf{a}_{v2} \cdot / \mathbf{a}_{v1})\|_2^2$  in (13) is used considering its good mathematical properties including: 1) it is convex and therefore enables a unique solution and 2) it balances well the penalty on a wide range of  $\mathbf{a}_{v2} \cdot / \mathbf{a}_{v1}$ . For any given  $j$ , the imposed penalty from the Logarithmic term  $\log^2(1 + a_{v2,j}/a_{v1,j})$  is calculated with different values of  $a_{v2,j}/a_{v1,j}$ . As shown in Fig. 2,  $\log^2(1 + a_{v2,j}/a_{v1,j})$  is close to zero given small values of  $a_{v2,j}/a_{v1,j}$ , denoting the regularization has minor influence on typical  $a_{v2,j}/a_{v1,j}$  that are relatively small. As  $a_{v2,j}/a_{v1,j}$  increases, the imposed regularization becomes stronger in order to suppress large perturbations in the retrieved temperature, such as the spike noise shown in Fig. 1. Therefore, it can be seen that the relative entropy regularization developed above is superior for keeping useful details of the reconstructed image while maintaining good performance on spike noise suppression.

By applying the relative entropy function  $g(\mathbf{a}_{v2}, \mathbf{a}_{v1})$  in (12), and retaining the empirical tuning parameter  $\mu$ , the inverse



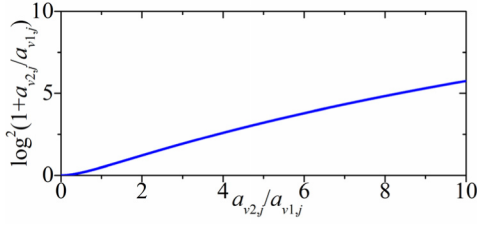


Fig. 2. Dependence of  $\log^2(1 + a_{v2,j}/a_{v1,j})$  on  $a_{v2,j}/a_{v1,j}$ .

problem of TDLAS tomography can be formulated as

$$\begin{aligned} \min_{\mathbf{a}_{v1}, \mathbf{a}_{v2}} & \left\{ \left\| \begin{bmatrix} \mathbf{A}_{v1} \\ \mathbf{0} \end{bmatrix} - \begin{bmatrix} \mathbf{L}\mathbf{a}_{v1} \\ \gamma \mathbf{F}\mathbf{a}_{v1} \end{bmatrix} \right\|_2^2 + \left\| \begin{bmatrix} \mathbf{A}_{v2} \\ \mathbf{0} \end{bmatrix} - \begin{bmatrix} \mathbf{L}\mathbf{a}_{v2} \\ \gamma \mathbf{F}\mathbf{a}_{v2} \end{bmatrix} \right\|_2^2 \right. \\ & \left. + \mu \|(\mathbf{a}_{v2} + \mathbf{a}_{v1}) \circ \log(1 + \mathbf{a}_{v2}/\mathbf{a}_{v1})\|_2^2 \right\} \\ \text{s.t. } & \mathbf{a}_{v1} > \mathbf{0}, \mathbf{a}_{v2} > \mathbf{0}. \end{aligned} \quad (14)$$

In general, the inverse problem in (14) can be solved by successive approximation of the convex regularization term  $\|(\mathbf{a}_{v2} + \mathbf{a}_{v1}) \circ \log(1 + \mathbf{a}_{v2}/\mathbf{a}_{v1})\|_2^2$ , which suffers from very high computational cost [28]. Alternatively, we recast (14) as a conic optimization problem

$$\begin{aligned} \min_{\mathbf{a}_{v1}, \mathbf{a}_{v2}, \boldsymbol{\tau}} & \left\{ \left\| \begin{bmatrix} \mathbf{A}_{v1} \\ \mathbf{0} \end{bmatrix} - \begin{bmatrix} \mathbf{L}\mathbf{a}_{v1} \\ \gamma \mathbf{F}\mathbf{a}_{v1} \end{bmatrix} \right\|_2^2 + \left\| \begin{bmatrix} \mathbf{A}_{v2} \\ \mathbf{0} \end{bmatrix} - \begin{bmatrix} \mathbf{L}\mathbf{a}_{v2} \\ \gamma \mathbf{F}\mathbf{a}_{v2} \end{bmatrix} \right\|_2^2 \right. \\ & \left. + \mu \sum_{j=1}^N \tau_j \right\} \\ \text{s.t. } & \mathbf{a}_{v1} > \mathbf{0}, \mathbf{a}_{v2} > \mathbf{0}, (\mathbf{a}_{v1} + \mathbf{a}_{v2}, \mathbf{a}_{v1}, \boldsymbol{\tau}) \in K_{\text{re}} \end{aligned} \quad (15)$$

where  $K_{\text{re}}$  is the (scalar) relative entropy cone defined by

$$\begin{aligned} K_{\text{re}} & \equiv \{(\mathbf{x}, \mathbf{y}, \boldsymbol{\tau}) \in \mathbb{R}_{++}^N \times \mathbb{R}_{++}^N \times \mathbb{R}_{++}^N : x_j \log(x_j/y_j) \leq \tau_j, \forall j\} \\ & \quad (16) \end{aligned}$$

and  $\boldsymbol{\tau} \in \mathbb{R}_{++}^N$  the auxiliary vector.

Consequently,  $\mathbf{a}_{v1}$  and  $\mathbf{a}_{v2}$  in (16) can be solved jointly and efficiently using the interior-point method [29], which is implemented by the MOSEK optimization suite for MATLAB [30]. With  $\mathbf{a}_{v1}$  and  $\mathbf{a}_{v2}$  in hand, the temperature image can be reconstructed by (10).

### III. NUMERICAL SIMULATION

In this section, the proposed RETRO algorithm is validated using numerical simulations of three phantoms with different numbers of inhomogeneities. The quality of the tomographic image was quantitatively examined in terms of image error, dislocation, accuracy of centroid value, and overshoot. To demonstrate the superiority of the proposed algorithm, its performance was compared with SART.

#### A. Simulation Setup

Water vapor ( $\text{H}_2\text{O}$ ) has a strong near-infrared absorption spectrum and is a principal product of hydrocarbon combustion. Therefore, it is selected as the target absorption species to demonstrate RETRO for TDLAS tomographic temperature imaging. The absorption transitions at  $\nu_1 = 7185.6 \text{ cm}^{-1}$  and  $\nu_2 = 7444.36 \text{ cm}^{-1}$  are used in this work. According to HITRAN 2016, they have moderate line strengths and good

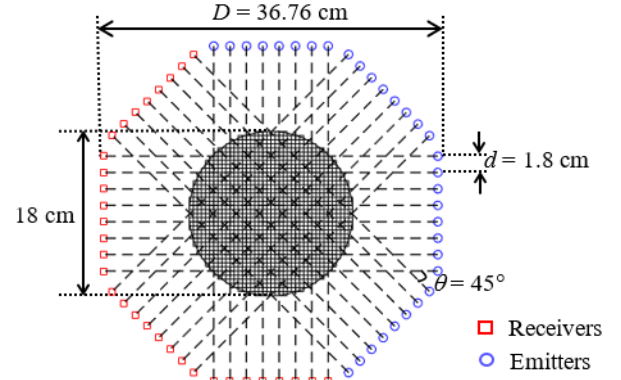


Fig. 3. Optical layout of the TDLAS tomographic sensor.

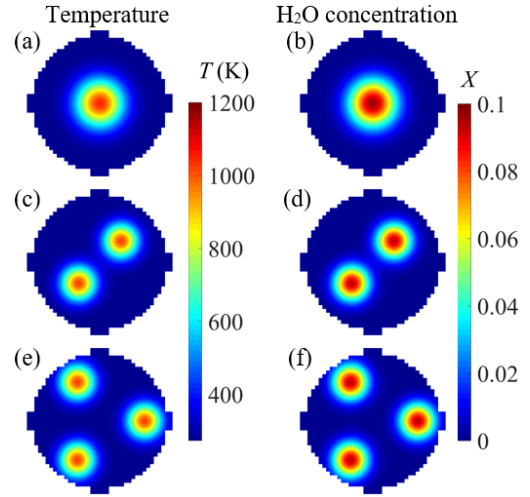


Fig. 4. Phantoms of 2-D distributions of temperature and  $\text{H}_2\text{O}$  concentration with (a) and (b) one, (c) and (d) two, and (e) and (f) three inhomogeneities, respectively.

temperature sensitivity over 300–1200 K [31]. Given no prior information of the target field, it has been shown that a regular beam array, i.e., equiangular projections and equispaced laser beams within each projection, leads to the uniform distribution of the sampling deficiency across the RoI [32]. Therefore, a parallel beam arrangement is adopted in this work, as shown in Fig. 3, with 32 laser beams arranged in four equiangular projection angles, each angle with eight equispaced parallel beams. The same optical layout is used for both the simulation and the experiment. In the experiment, all the optics and laser paths are enclosed and purified by dry air to avoid the ambient absorption.

The angular spacing between projections,  $\theta$ , is  $45^\circ$ . The neighboring beam spacing,  $d$ , is 1.8 cm, while the distance  $D$  between each emitter and detector is 36.76 cm. The central RoI is defined as a circular sensing area with a diameter of 18 cm that encloses the highest density of beam crossings, as shown in Fig. 3. The dimensions of each pixel in the RoI are  $0.45 \text{ cm} \times 0.45 \text{ cm}$ , resulting in 1396 uniformly segmented pixels.

Three phantoms of 2-D distributions of temperature and  $\text{H}_2\text{O}$  concentration are generated with one, two, and three inhomogeneities, respectively. As shown in Fig. 4, each

TABLE I  
SIMULATION PARAMETERS OF THE THREE PHANTOMS IN FIG. 4

	$(x_c^k, y_c^k)$ [cm]	$\sigma$ [cm]
Phantom 1	(0, 0)	0.9
Phantom 2	(-3.82, -3.82) (3.82, 3.82)	0.45
Phantom 3	(-2.7, 4.68) (2.7, -4.68) (5.4, 0)	0.45

inhomogeneity is simulated by a 2-D Gaussian profile. In a hydrocarbon flame, the  $H_2O$  concentration is generally well-correlated with the temperature. Therefore, the  $H_2O$  concentration distribution in each phantom is similar to the temperature distribution. The distributions of temperature and  $H_2O$  concentration are mathematically expressed as

$$T(x, y) = 298.15 + \sum_{k=1}^K 800 \exp \left[ -\frac{(x - x_c^k)^2 + (y - y_c^k)^2}{\sigma^2} \right] \quad (17)$$

$$X(x, y) = \sum_{k=1}^K 0.1 \exp \left[ -\frac{(x - x_c^k)^2 + (y - y_c^k)^2}{\sigma^2} \right] \quad (18)$$

where  $x$  and  $y$  denote the horizontal and vertical coordinates of the RoI, respectively.  $(x_c^k, y_c^k)$  is the central position of the  $k$ th Gaussian profile.  $\sigma$  is the standard deviation. Table I details the parameters of the three phantoms. A high-resolution RoI with 31 428 pixels, each with size  $0.09 \text{ cm} \times 0.09 \text{ cm}$ , is used in the phantoms to calculate the path integrals  $A_v$ . As a result, the forward problem in (3) can be formulated with high accuracy, thus facilitating the analysis of noise performance in Section III-C.

### B. Metrics for Image Quality Quantification

To examine the performance of the reconstruction algorithms, the tomographic images can be evaluated quantitatively using the following four metrics:

**Image Error (IE):** IE is defined as the relative error between the reconstructed and the true images, indicating the overall quality of the reconstructed image.

$$IE = \frac{\|T_{\text{rec}} - T_{\text{true}}\|_2}{\|T_{\text{true}}\|_2} \quad (19)$$

where  $T_{\text{rec}}$  and  $T_{\text{true}}$  represent the reconstructed and the true temperature distributions, respectively.

**Dislocation (DL):** DL characterizes the relative error of the centroid locations between the reconstructed inhomogeneity  $(x_r, y_r)$  and that of true inhomogeneity  $(x_c, y_c)$ . The centroid of the Gaussian-shaped inhomogeneity in the phantoms coincides with its center.

$$DL = \frac{\sqrt{(x_r - x_c)^2 + (y_r - y_c)^2}}{r_{\text{RoI}}} \quad (20)$$

where  $r_{\text{RoI}}$  is the radius of the RoI. For phantoms with multiple inhomogeneities, the mean value of DL is given below.

**Centroid Value Error (CVE):** CVE calculates the relative difference of temperature values at the centroids of the

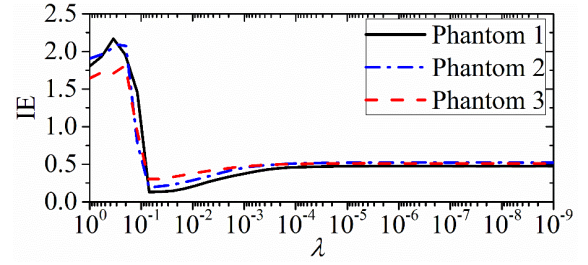


Fig. 5. Dependence of IE on  $\lambda$  in the SART.

reconstructed inhomogeneity  $T_{\text{rec}}(x_r, y_r)$  and that of the true inhomogeneity  $T_{\text{true}}(x_c, y_c)$ .

$$CVE = \frac{|T_{\text{rec}}(x_r, y_r) - T_{\text{true}}(x_c, y_c)|}{|T_{\text{true}}(x_c, y_c)|} \quad (21)$$

For phantoms with multiple inhomogeneities, the mean value of CVE is given below.

**Overshoot (OS):** OS is defined as the ratio of the number of pixels assessed as outliers,  $N_{\text{OT}}$ , to the total number of pixels,  $N$ .

$$OS = \frac{N_{\text{OT}}}{N} \quad (22)$$

In a window containing  $3 \times 3$  pixels, the mean temperature,  $\bar{T}_w$ , and the standard deviation,  $\sigma_w$ , is calculated. The outliers are defined as the pixels within the window with temperature values deviating from  $\bar{T}_w$  by more than  $3 \times \sigma_w$ .  $N_{\text{OT}}$  for a whole image is obtained from accumulating the number of outliers when the window moves across the RoI. Therefore, the extent of spike noise in the tomographic image can be characterized by OS.

### C. Determination of the Regularization Parameters

As noted in Section II, the regularization parameters play an important role in both SART and the proposed RETRO. One regularization parameter,  $\lambda$ , is involved in SART, while two,  $\gamma$  and  $\mu$ , are used in RETRO. In this section, these regularization parameters are optimally determined using the phantoms in Fig. 4. For other applications with very different phantoms, the regularization parameters can be determined by following the method detailed below.

In the simulation, the SNR of the LOS-TDLAS measurements was set to 40 dB, which is similar to the noise performance in the experiment. IE, the metric defined above to evaluate overall image quality, was calculated for all three phantoms when the regularization parameters were varied over wide ranges. For each given value of the regularization parameter, IE was averaged for 20 repeated simulations. The optimal regularization parameters were selected as those where the minimum value of the averaged IE was obtained, i.e., when the best image quality was achieved.

For SART, the averaged IE was calculated when  $\lambda$  varies from 1 to  $10^{-9}$  with 40 steps of logarithmic decrement. As shown in Fig. 5, the dependence of IE on  $\lambda$  follows the same trend for each of the three phantoms. IE decreases as  $\lambda$  decreases from 0.2. When  $\lambda$  equals 0.1, the minimal values

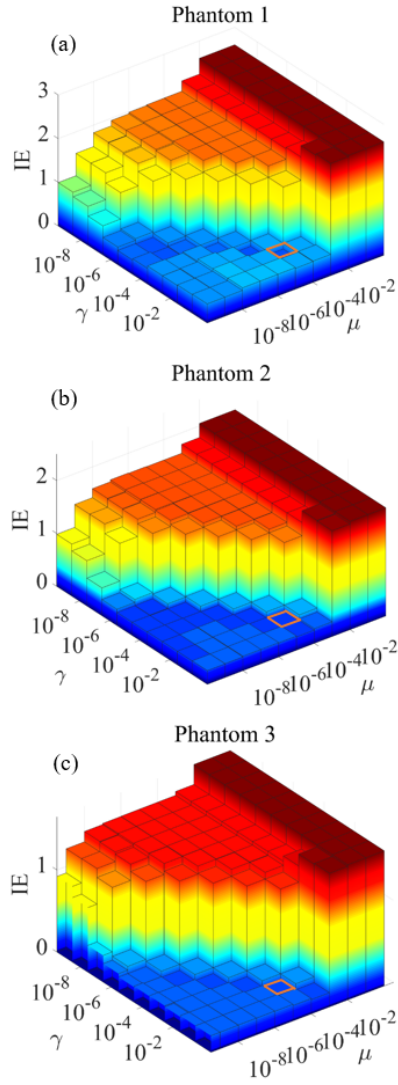


Fig. 6. Dependence of IE on  $\gamma$  and  $\mu$  for (a) phantom 1, (b) phantom 2, and (c) phantom 3 using the proposed RETRO algorithm. The optimal  $\gamma$  and  $\mu$  are 0.01 and  $10^{-5}$ , respectively.

of IE are 0.13, 0.19, and 0.28 for phantoms 1, 2, and 3, respectively. IE gradually increases as  $\lambda$  further decreases from 0.1. Therefore, the optimal  $\lambda$  is selected as 0.1 in SART.

For RETRO, the two regularization parameters  $\gamma$  and  $\mu$  were jointly evaluated to achieve the optimal image quality. For each phantom, the averaged IE was calculated for 100 different combinations of  $\gamma$  and  $\mu$  when each parameter varies from  $10^{-1}$  to  $10^{-9}$ . As shown in Fig. 6, relatively small values of IE can be obtained for all three phantoms within the parameter set  $\{(\mu, \gamma): \mu \leq 10^{-2}\gamma, 10^{-5} \leq \gamma \leq 10^{-1}, 10^{-6} \leq \mu \leq 10^{-2}\}$ . The optimal  $\gamma$  and  $\mu$  are 0.01 and  $10^{-5}$ , respectively, giving the values of IE 0.10, 0.12, and 0.14 for the three phantoms. This optimal combination of  $\gamma$  and  $\mu$  in RETRO is highlighted in Fig. 6.

#### D. Results and Discussion

With the regularization parameters determined above, both SART and RETRO were used to reconstruct simulated data

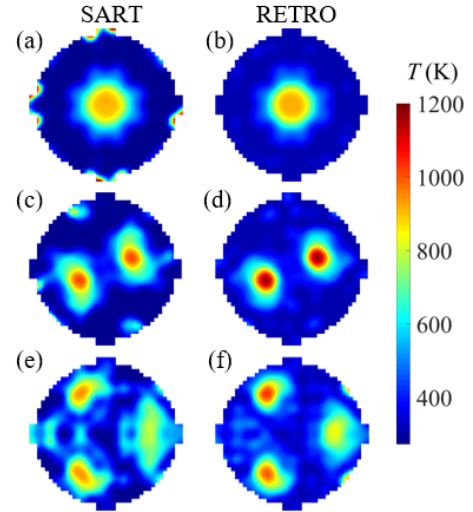


Fig. 7. Reconstructed temperature images using SART and the proposed RETRO algorithms with TDLAS tomographic data at the SNR of 40 dB for (a) and (b) phantom 1, (c) and (d) phantom 2, and (e) and (f) phantom 3, respectively.

TABLE II  
QUANTITATIVE EVALUATION OF THE SART AND THE PROPOSED RETRO USING THE FOUR METRICS, INCLUDING THE IMAGE ERROR (IE), DISLOCATION (DL), CENTROID VALUE ERROR (CVE), AND OVERSHOOT (OS)

		Phantom1	Phantom2	Phantom3
IE (%)	SART	14.7	23.6	31.8
	RETRO	10.1	12.3	16.9
DL (%)	SART	1.07	1.93	1.97
	RETRO	0.55	1.15	1.05
CVE (%)	SART	8.64	7.9	15.1
	RETRO	8.31	5.61	12.9
OS (%)	SART	2.35	1.92	4.17
	RETRO	1.53	1.17	1.06

from the three temperature images shown in Fig. 4. The simulation was first implemented with TDLAS tomographic data at the SNR of 40 dB. This work focuses on substantial improvement on temperature imaging in TDLAS tomography. The improved quality of temperature images will also contribute to a better accuracy of the gas concentration distributions that can be subsequently solved by linear tomographic algorithms [15].

Fig. 7 shows the three reconstructed temperature images. The proposed RETRO algorithm outperforms SART for all three phantoms. Although both algorithms are capable of locating and displaying the inhomogeneities, fewer artifacts are observed in the images reconstructed using RETRO.

To achieve quantitative validation of the proposed new algorithm, the four metrics described in Section II-B were calculated, with results presented in Table II. In terms of overall image quality, the proposed RETRO algorithm improves 4%–15% on IE compared with SART. In addition, RETRO is much superior in localizing inhomogeneities in the reconstructed temperature images since DL values obtained using RETRO, less than 1.2% for all three phantoms,



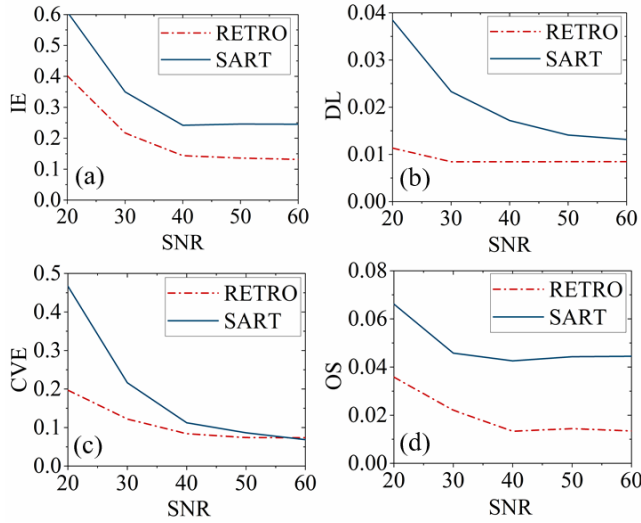


Fig. 8. Dependence of the four proposed metrics. (a) IE, (b) DL, (c) CVE, and (d) OS, on different SNRs for both SART and RETRO.

are approximately half of the values obtained using SART. A slightly better performance on CVE can be seen using RETRO, although both algorithms estimate temperature values at the centroids with all CVEs larger than 5%, arguably a poor level of accuracy. This is possibly caused by the regularization terms imposed on both algorithms, leading to robustness in image reconstruction at the cost of accuracy and bias errors in the retrieved temperature values. Finally, RETRO is much better at suppressing spike noise with smaller OS than those obtained using SART. In particular, OS for phantom 3 is 1.06% using the RETRO, which is approximately four times less than that using SART.

The performances of the two algorithms were evaluated further using simulated TDLAS measurements contaminated with different noise levels. The dependence of all the four metrics at different SNRs is shown in Fig. 8. For a given SNR, the value of each metric is averaged for the three phantoms. For the metrics of IE, DL, and OS, the results obtained using RETRO are persistently better than those using SART. For CVE, RETRO introduces more significant improvement in relatively low-SNR scenarios, which commonly exist in industrial field applications.

#### IV. EXPERIMENTAL VALIDATION

In this section, lab-scale experiments were carried out to further validate the proposed RETRO algorithm. The TDLAS tomographic sensor was built with the same optical layout as depicted in Fig. 3. The lasers at the transitions  $\nu_1 = 7185.6 \text{ cm}^{-1}$  and  $\nu_2 = 7444.36 \text{ cm}^{-1}$  were provided by two distributed feedback laser diodes NLK1E5GAAA and NLK1B5EAAA (NTT Electronics), respectively. Current modulation with a scan frequency  $f_s = 200 \text{ Hz}$  and a modulation frequency  $f_m = 40 \text{ kHz}$  was imposed on both laser diodes. With the time division multiplexing scheme between the two lasers, a temporal resolution of 10 ms can be achieved in the proof-of-concept experiment. The two laser diodes with pigtailed fibers were combined and split by a  $2 \times 32$  fiber

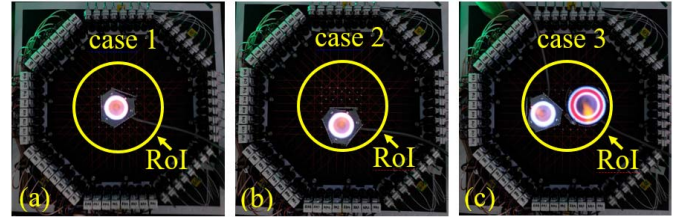


Fig. 9. Three temperature distributions generated in the experiment.

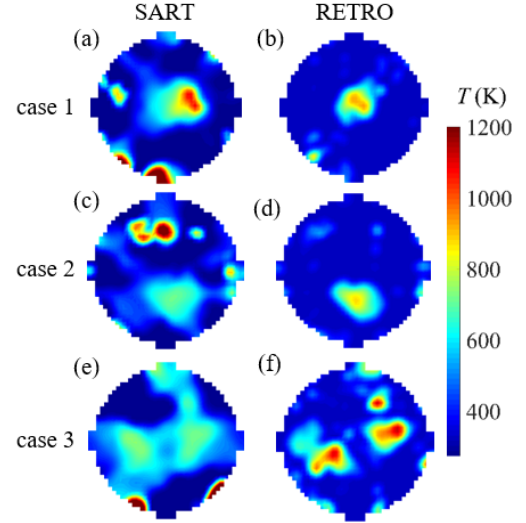


Fig. 10. Temperature images reconstructed using both SART and the proposed RETRO for (a) and (b) case 1, (c) and (d) case 2, and (e) and (f) case 3, respectively.

coupler to deliver the 32 laser beams in the tomographic sensor. Each collimated laser beam was detected by an InGaAs photodiode (G12182-010K, Hamamatsu) and then digitized by a data acquisition platform (RedPitaya) at 3.9 Mega Samples/second. Digital lock-in filters were used to extract the wavelength modulation spectroscopy (WMS) first and second harmonic signals, i.e.,  $1f$  and  $2f$ , from the transmitted signals. Finally, the calibration-free  $1f$  normalized  $2f$  signal, i.e.,  $\text{WMS-}2f/1f$  [33], [34], was fitted to calculate each of the 32 path integrals, i.e., the measured data, for each spectral transition.

In the experiment, three temperature distributions were generated to validate the proposed RETRO algorithm. As shown in Fig. 9, there is a single flame located at the center of the RoI in case 1. In case 2, the same flame is relocated at the lower center of the RoI. A more complex temperature profile with two flames in the RoI is used in case 3. Estimates of all three real temperature images were reconstructed from the same frame of measurement data using both RETRO and SART.

As shown in Fig. 10, the three temperature images reconstructed using RETRO have fewer artifacts and less spike noise than those using SART. For case 1, the location of the flame reconstructed using RETRO agrees well with the original one shown in Fig. 9(a), while that obtained from SART is distorted to the right of the center. The peak temperature values of the inhomogeneity retrieved by RETRO and SART in case 1 are 713 and 816 K, respectively. For case 2,

the relocated flame can be clearly localized using RETRO, the peak value of the retrieved temperature now being 683 K, similar to that in case 1. However, the temperature image in case 2 reconstructed by SART suffers from significant artifacts at the upper center of the RoI, showing an unreal high-temperature inhomogeneity with maximum temperature value of 1159 K. In addition, the peak temperature value of the real inhomogeneity reconstructed using SART is 574 K, an offset of 242 K compared with that in case 1. For case 3, RETRO can reliably resolve the two flames with their locations being consistent with those in the real temperature distribution. However, the boundaries of the flames retrieved by SART are severely blurred with much lower temperature values.

## V. CONCLUSION

In this article, we developed a radically new reconstruction algorithm for high-fidelity temperature imaging in TDLAS tomography, called the RETRO algorithm. RETRO enables temperature retrieval from the jointly reconstructed two-line absorbance distributions, thus significantly suppressing the spike noise caused by the ill-posed nature of TDLAS tomography. RETRO was analytically demonstrated to be successful in retaining useful details of the reconstructed temperature image while maintaining good robustness against noise.

The performance of the proposed RETRO algorithm was compared with the SART algorithm, by simulation and by experiment, using two H<sub>2</sub>O transitions and a fixed beam arrangement. The regularization parameters for both algorithms were optimized using noise-contaminated data with the SNR of 40 dB. Four metrics were proposed to evaluate quantitatively the performances of both algorithms. For a wide range of measurement SNR, simulation results indicate that RETRO can reconstruct the temperature images for the three phantoms used with better quality in comparison with SART. In the experiment, both algorithms were used to reconstruct three different temperature distributions. Compared with those obtained using SART, the tomographic temperature images using RETRO achieved much better agreement with the known locations of the original flames and have stronger resistance to spike noise.

In summary, both simulation and experiment indicate that the proposed new RETRO algorithm for two-line temperature tomography is spatially accurate and robust to noisy measurements and is superior to well-established algorithms for TDLAS tomography. These attributes are invaluable for implementations in harsh environments. In our future work, the RETRO algorithm will be enhanced to incorporate the redundancy of temporal information to investigate the dynamic evolution of the flame.

## ACKNOWLEDGMENT

The authors would like to thank Dr. Nick Polydorides for his useful suggestions.

## REFERENCES

- [1] F. P. Hindle, S. J. Carey, K. Ozanyan, D. E. Winterbone, E. Clough, and H. McCann, "Measurement of gaseous hydrocarbon distribution by a near-infrared absorption tomography system," *J. Electron. Imag.*, vol. 10, no. 3, pp. 593–600, 2001.
- [2] Z. Wang *et al.*, "Two-dimensional temperature measurement in a high-temperature and high-pressure combustor using computed tomography tunable diode laser absorption spectroscopy (CT-TDLAS) with a wide-scanning laser at 1335–1375 nm," *Appl. Spectrosc.*, vol. 74, no. 2, pp. 210–222, Feb. 2020.
- [3] W. Zhao *et al.*, "A WMS based TDLAS tomographic system for distribution retrievals of both gas concentration and temperature in dynamic flames," *IEEE Sensors J.*, vol. 20, no. 8, pp. 4179–4188, Apr. 2020.
- [4] C. Liu, Z. Cao, Y. Lin, L. Xu, and H. McCann, "Online cross-sectional monitoring of a swirling flame using TDLAS tomography," *IEEE Trans. Instrum. Meas.*, vol. 67, no. 6, pp. 1338–1348, Jun. 2018.
- [5] L. Ma *et al.*, "50-kHz-rate 2D imaging of temperature and H<sub>2</sub>O concentration at the exhaust plane of a J85 engine using hyperspectral tomography," *Opt. Express*, vol. 21, no. 1, pp. 1152–1162, 2013.
- [6] N. Terzija, S. Karagiannopoulos, S. Begg, P. Wright, K. Ozanyan, and H. McCann, "Tomographic imaging of the liquid and vapour fuel distributions in a single-cylinder direct-injection gasoline engine," *Int. J. Engine Res.*, vol. 16, no. 4, pp. 565–579, 2015.
- [7] S.-A. Tsekenis, K. G. Ramaswamy, N. Tait, Y. Hardalupas, A. Taylor, and H. McCann, "Chemical species tomographic imaging of the vapour fuel distribution in a compression-ignition engine," *Int. J. Engine Res.*, vol. 19, no. 7, pp. 718–731, Sep. 2018.
- [8] C. F. Kaminski, "A tomographic technique for the simultaneous imaging of temperature, chemical species, and pressure in reactive flows using absorption spectroscopy with frequency-agile lasers," *Appl. Phys. Lett.*, vol. 104, no. 3, Jan. 2014, Art. no. 034101.
- [9] M. P. Wood and K. B. Ozanyan, "Simultaneous temperature, concentration, and pressure imaging of water vapor in a turbine engine," *IEEE Sensors J.*, vol. 15, no. 1, pp. 545–551, Jan. 2015.
- [10] Q. Qu, Z. Cao, L. Xu, C. Liu, L. Chang, and H. McCann, "Reconstruction of two-dimensional velocity distribution in scramjet by laser absorption spectroscopy tomography," *Appl. Opt.*, vol. 58, no. 1, pp. 205–212, 2019.
- [11] C. Liu and L. Xu, "Laser absorption spectroscopy for combustion diagnosis in reactive flows: A review," *Appl. Spectrosc. Rev.*, vol. 54, no. 1, pp. 1–44, Jan. 2019.
- [12] S. J. Grauer, J. Emmert, S. T. Sanders, S. Wagner, and K. J. Daun, "Multiparameter gas sensing with linear hyperspectral absorption tomography," *Meas. Sci. Technol.*, vol. 30, no. 10, Art. no. 105401, 2019.
- [13] W. Cai and C. F. Kaminski, "Tomographic absorption spectroscopy for the study of gas dynamics and reactive flows," *Prog. Energy Combustion Sci.*, vol. 59, pp. 1–31, Mar. 2017.
- [14] K. J. Daun, S. J. Grauer, and P. J. Hadwin, "Chemical species tomography of turbulent flows: Discrete ill-posed and rank deficient problems and the use of prior information," *J. Quant. Spectrosc. Radiat. Transf.*, vol. 172, pp. 58–74, 2016.
- [15] H. Xia *et al.*, "Two-step tomographic reconstructions of temperature and species concentration in a flame based on laser absorption measurements with a rotation platform," *Opt. Lasers Eng.*, vol. 90, pp. 10–18, Mar. 2017.
- [16] T. Yu and W. Cai, "Benchmark evaluation of inversion algorithms for tomographic absorption spectroscopy," *Appl. Opt.*, vol. 56, no. 8, pp. 2183–2194, 2017.
- [17] C. Liu, L. Xu, J. Chen, Z. Cao, Y. Lin, and W. Cai, "Development of a fan-beam TDLAS-based tomographic sensor for rapid imaging of temperature and gas concentration," *Opt. Express*, vol. 23, no. 17, pp. 22494–22511, 2015.
- [18] K. J. Daun, "Infrared species limited data tomography through tikhonov reconstruction," *J. Quant. Spectrosc. Radiat. Transf.*, vol. 111, no. 1, pp. 105–115, Jan. 2010.
- [19] E. M. D. Fisher *et al.*, "A custom, high-channel count data acquisition system for chemical species tomography of aero-jet engine exhaust plumes," *IEEE Trans. Instrum. Meas.*, vol. 69, no. 2, pp. 549–558, Feb. 2020.
- [20] Y. Deguchi *et al.*, "Applications of laser diagnostics to thermal power plants and engines," *Appl. Thermal Eng.*, vol. 73, no. 2, pp. 1453–1464, Dec. 2014.
- [21] S. J. Grauer, P. J. Hadwin, and K. J. Daun, "Bayesian approach to the design of chemical species tomography experiments," *Appl. Opt.*, vol. 55, no. 21, pp. 5772–5782, 2016.
- [22] S. J. Grauer, P. J. Hadwin, and K. J. Daun, "Improving chemical species tomography of turbulent flows using covariance estimation," *Appl. Opt.*, vol. 56, no. 13, pp. 3900–3912, 2017.
- [23] A. C. Kak, M. Slaney, and G. Wang, "Principles of computerized tomographic imaging," *Med. Phys.*, vol. 29, no. 1, p. 107, 2002.
- [24] J. Nocedal and S. J. Wright, *Numerical Optimization*. New York, NY, USA: Springer, 2006.



- [25] M. Grant, S. Boyd, and Y. Ye, "Disciplined convex programming," in *Global Optimization* (Nonconvex Optimization and Its Applications), vol. 84, L. Liberti and N. Maculan, Eds. Boston, MA, USA: Springer, 2006, doi: [10.1007/0-387-30528-9\\_7](https://doi.org/10.1007/0-387-30528-9_7).
- [26] S. Boyd, S. P. Boyd, and L. Vandenberghe, *Convex Optimization*. Cambridge, U.K.: Cambridge Univ. Press, 2004.
- [27] V. Chandrasekaran and P. Shah, "Relative entropy optimization and its applications," *Math. Program.*, vol. 161, nos. 1–2, pp. 1–32, Jan. 2017.
- [28] H. Fawzi, J. Saunderson, and P. A. Parrilo, "Semidefinite approximations of the matrix logarithm," *Found. Comput. Math.*, vol. 19, no. 2, pp. 259–296, Apr. 2019.
- [29] Y. E. Nesterov and A. S. Nemirovski, *Interior Point Polynomial Algorithms in Convex Programming*. Philadelphia, PA, USA: SIAM, 1994.
- [30] E. D. Andersen and K. D. Andersen, "The mosek interior point optimizer for linear programming: An implementation of the homogeneous algorithm," in *High Performance Optimization* (Applied Optimization), vol. 33, H. Frenk, K. Roos, T. Terlaky, and S. Zhang, Eds. Boston, MA, USA: Springer, 2000, doi: [10.1007/978-1-4757-3216-0\\_8](https://doi.org/10.1007/978-1-4757-3216-0_8).
- [31] C. Liu, L. Xu, Z. Cao, and H. McCann, "Reconstruction of axisymmetric temperature and gas concentration distributions by combining fan-beam TDLAS with onion-peeling deconvolution," *IEEE Trans. Instrum. Meas.*, vol. 63, no. 12, pp. 3067–3075, Dec. 2014.
- [32] C. Liu, S.-A. Tsekenis, N. Polydorides, and H. McCann, "Toward customized spatial resolution in TDLAS tomography," *IEEE Sensors J.*, vol. 19, no. 5, pp. 1748–1755, Mar. 2019.
- [33] C. S. Goldenstein, C. L. Strand, I. A. Schultz, K. Sun, J. B. Jeffries, and R. K. Hanson, "Fitting of calibration-free scanned-wavelength-modulation spectroscopy spectra for determination of gas properties and absorption lineshapes," *Appl. Opt.*, vol. 53, no. 3, pp. 356–367, 2014.
- [34] T. Benoy, D. Wilson, M. Lengden, I. Armstrong, G. Stewart, and W. Johnstone, "Measurement of CO<sub>2</sub> concentration and temperature in an aero engine exhaust plume using wavelength modulation spectroscopy," *IEEE Sensors J.*, vol. 17, no. 19, pp. 6409–6417, Oct. 2017.



**Yong Bao** (Member, IEEE) received the B.Sc. degree in digital communications from the Dalian University of Technology, Dalian, China, in 2014, and the M.Sc. and Ph.D. degrees in digital communications from The University of Edinburgh, Edinburgh, U.K., in 2015 and 2019, respectively.

From September, he joined the Agile Tomography Group, IDCOM, The University of Edinburgh, as a Research Associate. His research interests include acoustic signal processing, acoustic travel-time tomography, and TDLAS-based tomography.



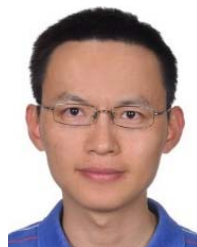
**Rui Zhang** received the B.Eng. degree (Hons.) in electronics and electrical engineering with management from The University of Edinburgh, Edinburgh, U.K., and the B.Eng. degree (Hons.) in internet of things engineering from Tianjin University, Tianjin, China, in 2019. She is currently pursuing the Ph.D. degree with the Agile Tomography Group, School of Engineering, The University of Edinburgh.

Her current research interest is focused on laser absorption spectroscopic tomography with a customized spatial resolution for combustion diagnosis.



**Godwin Enemali** (Member, IEEE) received the B.Eng. degree (Hons.) in electrical and electronics engineering from the University of Agriculture Makurdi, Makurdi, Nigeria, in 2010, and the M.Sc. and Ph.D. degrees in electronics engineering from The University of Edinburgh, Edinburgh, U.K., in 2014 and 2019, respectively.

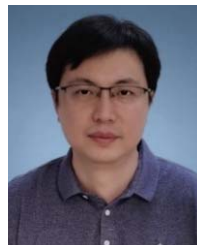
Since 2019, he has been a Research Associate with the Agile Tomography Group, Institute for Digital Communication, The University of Edinburgh. His current research focuses on high-speed data acquisition systems, reliable FPGA-based system implementation, laser absorption spectroscopy (LAS), and chemical species tomography.



absorption tomography, multiphase flow measurement, and inverse problems.

**Zhang Cao** (Member, IEEE) received the B.Sc. degree (with distinction) in automation and the M.Eng. and Ph.D. degrees (with distinction) in measurement technology and automatic devices from Tianjin University, Tianjin, China, in 2003, 2005, and 2008, respectively.

From 2008, he works for Beihang University, Beijing, China. He is currently a Professor with the School of Instrumentation Science and Opto-Electronic Engineering, Beihang University, Beijing, China. His research interests include laser



**Bin Zhou** received the B.Sc. and Ph.D. degrees from Southeast University, Nanjing, China, in 2002 and 2008, respectively.

He is currently an Associate Professor with Southeast University, where he is the Vice Dean of the Jiang Bei Innovation Center. His current research interests include NIR/MIR laser absorption spectroscopy (LAS), electrical capacitance tomography (ECT), and their applications to combustion diagnosis and industrial application.



**Hugh McCann** received the B.Sc. and Ph.D. degrees from the University of Glasgow, Glasgow, U.K., in 1976 and 1980, respectively.

He was the Head of the School of Engineering, The University of Edinburgh, Edinburgh, U.K., from 2013 to 2018, where he is currently a Professor of tomographic imaging. He was a Professor of industrial tomography at the University of Manchester, Manchester, U.K., from 1996 to 2013, following ten years in Research and Development at the Royal Dutch/Shell Group. He was involved in high-energy particle physics for ten years at Glasgow, Manchester, CERN (Geneva, Switzerland) and DESY (Hamburg, Germany). He has extended industrial tomography to provide specific chemical contrast using high-speed all-opto-electronic techniques, and has developed electrical impedance tomography for medical applications, collaborating intensively with users in both academia and industry. He was the Head of the School of Electrical and Electronic Engineering at Manchester from 1999 to 2002 and the Chair of the U.K. Professor and Heads of Electrical Engineering from 2003 to 2005. In 2018, he was appointed Honorary Professor at Beihang University, Beijing, China.

Dr. McCann was elected a fellow of the Royal Academy of Engineering in 2009 and the Royal Society of Edinburgh in 2015.



**Chang Liu** (Member, IEEE) received the B.Sc. degree in automation from Tianjin University, Tianjin, China, in 2010, and the Ph.D. degree in testing, measurement technology, and instrument in Beihang University, Beijing, China, in 2016.

From April 2016 to January 2018, he was a Post-Doctoral Researcher with the Department of Air Pollution and Environmental Technology, Empa-Swiss Federal Laboratories for Materials Science and Technology, Dübendorf, Switzerland. From February 2018, he has been a Lecturer with the School of Engineering, University of Edinburgh, Edinburgh, U.K. His current research interests include NIR/MIR laser absorption spectroscopy (LAS), active/passive optical tomography techniques and system design, and their applications to combustion diagnosis and environmental monitoring.